Vietnam Journal of Earth Sciences, 1–30, https://doi.org/10.15625/2615-9783/25119

Vietnam Journal of Earth Sciences
https://vjs.ac.vn/index.php/jse



A data-driven workflow for constructing depth-dependent rock-physics templates for the Oligocene D Formation in the Cuu Long Basin, offshore Vietnam

Nguyen Danh Lam[1*], Ta Quang Minh[1], Pham The Hoang Ha[1], Nguyen Thanh Tung[1], Nguyen Thi Thanh[1], Ha Quoc Dat[1], Nguyen Trung Hieu[1], Nguyen Phuong Thuy[2], Phan Thien Huong[3], Le Trung Nguyen[4]

[1]*Vietnam Petroleum Institute, 167 Trung Kinh Street, Yen Hoa, Hanoi, Vietnam*
[2]*Murphy Oil Corporation, Level 35, Bitexco Financial Tower, HCMC, Vietnam*
[3]*Hanoi University of Mining and Geology, Pho Vien Street, Tu Liem, Hanoi, Vietnam*
[4]*Viridien, Crompton Way, Manor Royal Estate, Crawley, West Sussex, RH10 9QN, United Kingdom*

Received 29 May 2026; Received in revised form 15 June 2026; Accepted 26 August 2026

ABSTRACT

Rock physics templates are widely used to link seismic elastic attributes with lithology, porosity, and pore-fluid effects. However, their application becomes uncertain where elastic responses vary systematically with burial depth, especially where laboratory-derived rock-frame parameters are unavailable. This study presents a data-driven workflow for constructing depth-dependent rock physics templates for the Oligocene D Formation reservoir interval in the Cuu Long Basin, offshore Vietnam. The workflow integrates well-log-derived elastic properties, petrophysical interpretation, core and composite-log information, and lithology interpretation from 15 wells. Measured logs, including Gamma Ray (GR), compressional wave slowness (DTC), shear wave slowness (DTS), bulk density (RHOB), water saturation, total porosity, and effective porosity, were used to calculate P-impedance (AI), compressional wave to shear wave velocity ratio (Vp/Vs), and saturated elastic moduli. Instead of relying on fixed laboratory-derived rock-physics parameters, matrix and dry-frame elastic moduli were estimated through a nonlinear optimization scheme by minimizing the mismatch between modeled and logged saturated bulk and shear moduli. The calibrated parameters were then used to generate rock physics templates in the P-impedance versus Vp/Vs domain for different depth intervals. Three key findings obtained from representative wells show that: (i) A single template cannot adequately describe the full D Formation interval because compaction, lithological variation, and shale volume shift the elastic trends with depth; (ii) Depth-calibrated templates improve separation of clean sand, shaly sand, and shale, and better capture porosity variations compared with a single generalized template; and (iii) A preliminary geostatistical interpolation of optimized elastic parameters suggests that depth-dependent templates can be extended beyond wells and enhance lithology and porosity prediction in seismic inversion workflows.

Keywords: Rock physics template, lithology prediction, Oligocene, Cuu Long Basin, D reservoir.

1. Introduction

Rock physics templates (RPTs) provide a practical bridge between seismic elastic attributes and reservoir properties such as lithology, porosity, and pore-fluid content. In a typical application, well-log observations and rock-physics models are displayed in an elastic-attribute domain, commonly acoustic

*Corresponding author, Email: lamnd@vpi.pvn.vn

impedance (AI) versus Vp/Vs ratio. Consequently, seismic inversion results can be interpreted in terms of geological and petrophysical classes (Avseth & Ødegaard, 2004; Avseth et al., 2005; Mavko et al., 2009). RPTs therefore play an important role in quantitative seismic interpretation, particularly in regions with insufficient data.

The construction of an RPT normally requires assumptions about mineral moduli, fluid properties, dry-frame stiffness, and the manner in which porosity, lithology, and saturation affect the elastic response. These parameters are commonly calibrated using laboratory measurements, core analysis, or established rock-physics models such as Voigt-Reuss-Hill mixing, Hertz-Mindlin contact theory, Hashin-Shtrikman bounds, and Gassmann fluid substitution (Mavko & Mukerji, 1995; Kuster & Toksoz, 1974; Hill, 1963). The main research gap addressed in this study is not simply the shortage of laboratory-derived elastic parameters, but the lack of a robust calibration strategy for RPT construction in heterogeneous clastic successions where rock-frame properties vary with stratigraphy, depth, compaction and shale content. In such settings, a single compaction trend or a fixed set of rock-physics parameters may oversimplify the elastic background, leading to significant overlap among shale, shaly sand, and reservoir sand. This study therefore proposes an interval-dependent RPT workflow in which effective matrix and dry-frame parameters are calibrated from well logs and petrophysical data and updated for different stratigraphic/depth intervals of the D Formation.

Previous studies have shown that RPTs are sensitive to burial history, pressure, cementation, pore geometry, mineral composition, porosity, and fluid type (Avseth et al., 2014; Johansen et al., 2013; Dræge, 2010). As burial depth increases, compaction and diagenesis can shift impedance and Vp/Vs trends, causing similar lithologies to occupy different positions in the elastic domain. Conversely, different lithologies or fluid states may overlap in a single crossplot when one generalized template is applied to a thick stratigraphic interval. These effects can lead to ambiguous interpretations of lithology and porosity if the depth-dependent elastic background is not explicitly accounted for.

Regarding the geological study area, D Formation in this paper refers to the Oligocene D Formation interval of the Cuu Long Basin, offshore southeastern Vietnam. The interval is composed mainly of interbedded sandstones, siltstones, and shales deposited in a lacustrine to rift-related setting. Although it was previously regarded mainly as a source-rock succession, recent drilling results demonstrate that sand-prone intervals occur within D Formation and may form reservoirs. Vertical heterogeneity, variable shale volume, burial-depth effects, and local structural relief complicate its elastic response. In the available dataset, no single rock-physics model adequately separates lithology and porosity across the full interval. In addition, the same AI and Vp/Vs values may correspond to different lithological interpretations at different depth levels.

This study develops a data-driven framework for constructing depth-dependent RPTs from well-log observations. Instead of relying only on fixed laboratory-derived parameters, the workflow estimates matrix and dry-frame elastic parameters by optimizing the mismatch between modeled and log-derived saturated moduli. The calibrated parameters are then used to generate RPTs for different depth windows and to evaluate their ability to predict lithology and porosity. The main objectives are: (1) to quantify how RPTs vary with depth in D Formation; (2) to demonstrate the improvement obtained by using depth-calibrated templates rather than a single

generalized template; and (3) to test the potential for extending optimized rock-physics parameters away from wells through preliminary geostatistical interpolation.

2. Geological and tectonic setting

The Cuu Long Basin is a prolific hydrocarbon basin located offshore southeastern Vietnam. Its development is related to the regional tectonic evolution of Southeast Asia, including rifting, local compression or inversion, and subsequent thermal subsidence. Nguyen Thi Mai et al. (2022) showed that the South-Central Vietnam continental shelf and adjacent areas are influenced by major fault systems, including the 109° Meridian fault and associated NE-SW-trending faults, which help separate major Cenozoic basins such as the Cuu Long, Nam Con Son and Tu Chinh-Vung May basins. Pubellier and Sautter (2022) further discussed key structural elements around the East Vietnam Sea and their implications for regional tectonic reconstructions. These regional studies support the interpretation that the Cuu Long Basin developed within a structurally complex continental-margin setting, where faulting, subsidence and later tectonic reactivation may influence burial history, stratigraphic architecture and elastic properties. Basin evolution has commonly been divided into an Eocene-to-early Oligocene rifting phase, a mid-to-late Oligocene compression and inversion phase, and a late Oligocene-to-present thermal subsidence phase (Schmidt et al., 2019). Viet et al. (2012) described the Cenozoic tectonic development of the basin as a multi-stage process closely related to active fault systems and regional geodynamics. They divided the basin evolution into three main stages, including a Middle Eocene to Late Oligocene stage characterized by extensional phases followed by compression, during which sub-basins were formed, later linked into a larger central lacustrine depocentre, and locally affected by anticlinal structures. This tectonic framework is important for the present study because Formation D was deposited during a period of active subsidence, fault development and local inversion, which may have influenced burial depth, compaction state and elastic properties.

Formation D was deposited during the transition from transtensional rifting to transpression. The lower and middle parts of the sequence accumulated mainly within accommodation space generated by normal faulting. Up-section, the structural style changed as rifting waned and transpression became more important. This transition is expressed by compressional folding, reactivation of normal faults, and localized unconformities over uplifted structural highs. D Formation was deposited during the transition from transtensional rifting to transpression. The lower and middle parts of the sequence accumulated mainly within accommodation space generated by normal faulting. Up-section, the structural style changed as rifting waned and transpression became more important. This transition is expressed by compressional folding, reactivation of normal faults, and localized unconformities over uplifted structural highs.

The interval was previously regarded mainly as a source-rock succession composed of fine-grained siltstone and shale deposited in a lacustrine environment (Breitfeld et al., 2022). Mai Thanh et al. (2024) documented Oligocene continental sediments in several northern Vietnamese Cenozoic basins, including conglomerate, sandstone, siltstone, claystone and coal shale, using petrographic, X-ray diffraction and palynological data. Although these basins are not direct analogs of the Cuu Long Basin, the study provides useful regional evidence that Oligocene successions in Vietnam may be lithologically heterogeneous and influenced by depositional

environment and paleoclimate. This supports treating Formation D as an interval with variable lithology, clay content, and petrophysical properties rather than as a single homogeneous rock-physics unit. More recent drilling results, however, demonstrate that sand-prone intervals occur within D Formation and may form reservoirs. The coexistence of sand, shaly sand, and shale, together with variable burial depth and structural relief, makes D Formation suitable for testing a depth-dependent RPT approach.

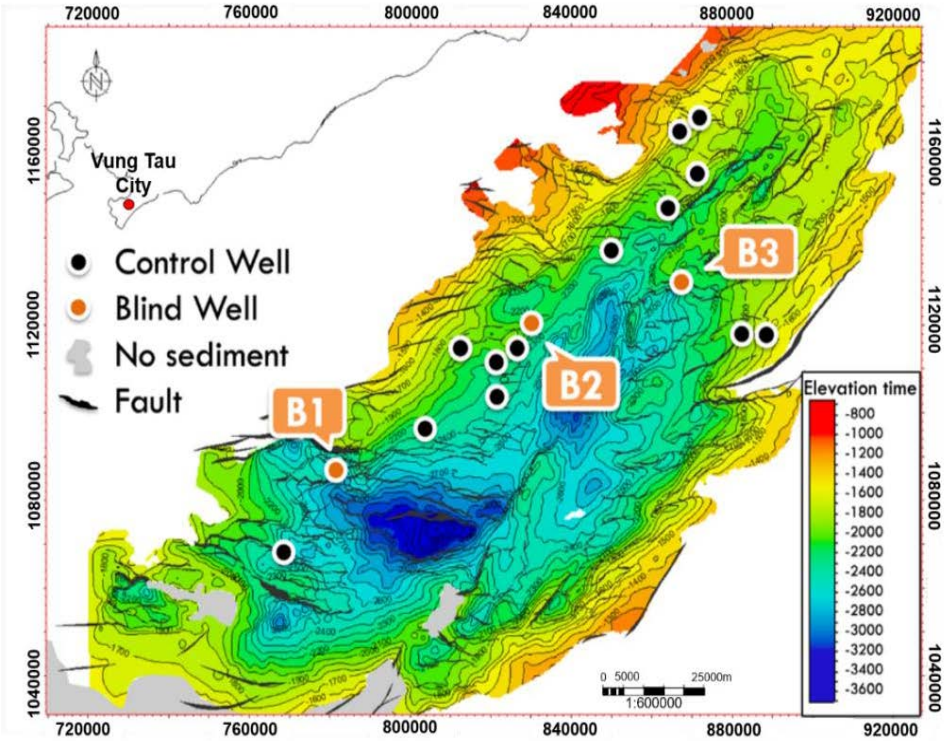


Figure 1. Structural depth map of the top D, with spatial distribution of 15 wells and 3 blind-test wells used for Drift Kriging interpolation of optimized RPT elastic parameters

Morley et al. (2019) demonstrated that the Oligocene succession of the Cuu Long Basin consists of repeated high-frequency depositional cycles, calibrated using biostratigraphy and seismic data. This indicates that D Formation should not be treated as a homogeneous rock-physics interval. In addition, Mai Hoang Dam et al. (2023) showed that Sequence D of the Lower Tra Tan Formation can be subdivided into three parasequences with different depositional and petrographic characteristics, ranging from lake-margin swamp to shallow lacustrine settings. Sequence D is characterized by poor to fair porosity, with reservoir quality controlled by detrital matrix, authigenic minerals, compaction, and burial depth. These findings provide a geological justification for constructing multiple interval-dependent RPTs for the D Formation rather than applying a single generalized template.

3. Data and methods

3.1. Dataset and petrophysical classification

The study uses data from 15 wells that penetrate the Oligocene D Formation. The well distribution is shown on the structural depth map of the top of the D Formation

(Fig. 1). For each well, the available logs include gamma ray (GR), P-wave slowness (DTC), S-wave slowness (DTS), bulk density (RHOB), water saturation, total porosity, and effective porosity. Elastic attributes such as P-wave velocity, S-wave velocity, P-impedance, Vp/Vs, saturated bulk modulus, and saturated shear modulus were calculated from these measured logs.

The lithology assignment should be constrained by integrating multiple logs and geological evidence, where available (Serra, 1986; Rider et al., 2011; Asquith and Krygowski, 2004). Core descriptions, cutting descriptions, mud-log information, master logs, and composite logs were used, where available, to constrain lithology at well locations. These geological observations were combined with log-pattern analysis and petrophysical interpretation to classify the main lithologies within D Formation. This follows standard well-log interpretation practice, in which lithology and porosity are not assigned from a single log curve but from the combined response of multiple logs calibrated against geological evidence (Schlumberger, 1991; Serra, 1986; Rider et al., 2011; Asquith and Krygowski, 2004; Ellis and Singer, 2007).

In the study area, the interval is dominated by sand, shaly sand and shale, with several volcanic rock intervals locally identified. The volcanic rocks are characterized by very low gamma-ray values, low sonic-log values, high density values and relatively low neutron-log responses.

The lithology was interpreted using the combined response of multiple well logs rather than relying on a single log. In particular, the neutron-density log combination is one of the most useful lithology indicators for many formations, because both neutron and density logs respond to the same primary formation parameter, namely porosity. When plotted on compatible porosity scales, the two curves should yield comparable values and can be superimposed for interpretation (Rider et al., 2011). Neutron and density log responses can also be used quantitatively to support lithology identification.

Figure 2a illustrates the lithology interpretation workflow for a representative well interval. The figure compares gamma-ray, deep resistivity, neutron-density, sonic, interpreted lithology from well data, and lithology described in the master log. The interpreted lithology shows good agreement with the master-log description over the example interval of 3150–3230 mMD, indicating that the well-log-based lithology classification is consistent with direct geological observations. The neutron-density crossplot in the same figure provides additional verification of lithology separation, particularly between sand, shaly sand, and shale.

Core data were used to validate well-log interpretations when available. Figure 2b compares core-derived gamma-ray and porosity measurements with the corresponding well-log responses and interpreted petrophysical properties. The example from the 2785.0–2822.4 mMD interval shows a good correlation between depth-shifted core gamma-ray data and the well-log gamma-ray curve, as well as between core porosity and log-derived effective porosity. This comparison supports the reliability of the log-based lithology and porosity interpretation used for rock-physics analysis.

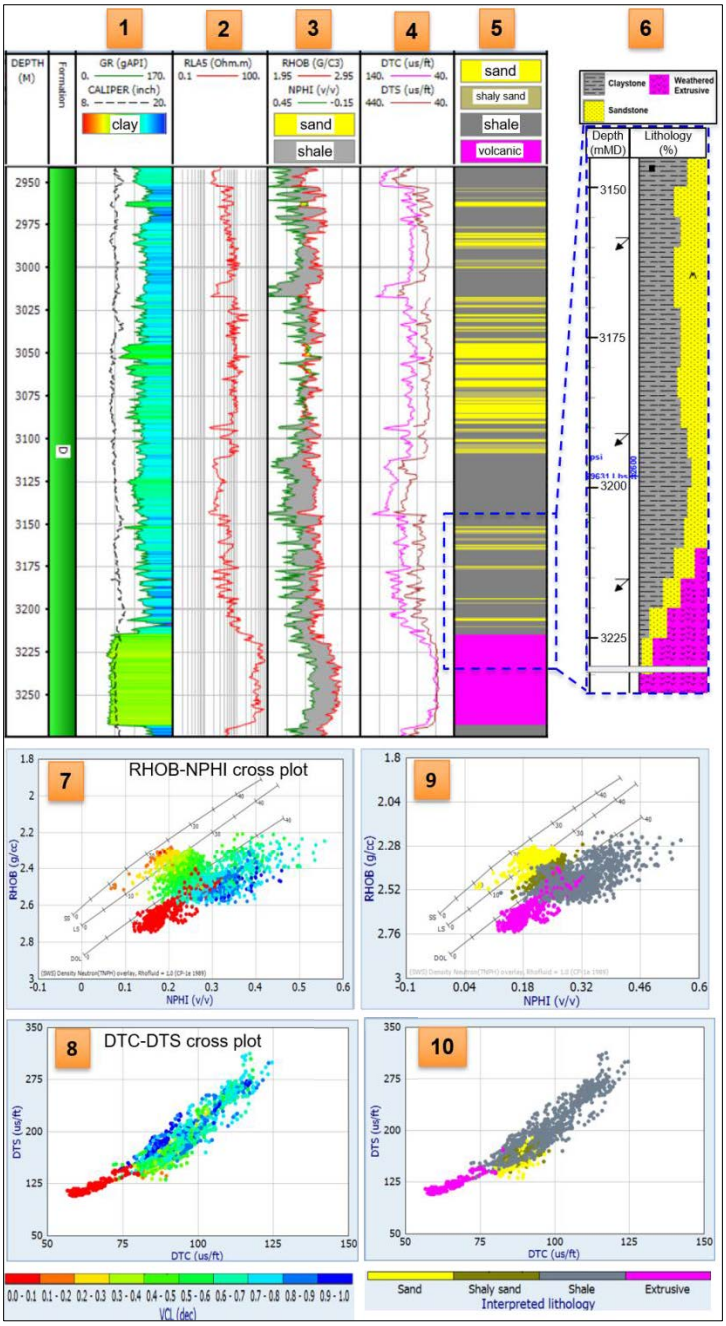


Figure 2a. Lithology interpretation based on a combination of well data. (1) Gamma Ray (2) Deep resistivity (3) Neutron-density log (4) Sonic logs (5) interpreted lithology from well data (6) Lithology described from master log is used to calibrate interpreted lithology. For example, over the interval of 3150–3230 mMD, the interpreted lithology shows good agreement with the lithology described in the master log; Neutron-density and DTC-DTS cross plots, which are colored by clay volume (7), (8) and interpreted lithology (9), (10) respectively, illustrate good consistency between the interpreted lithology and well log responses

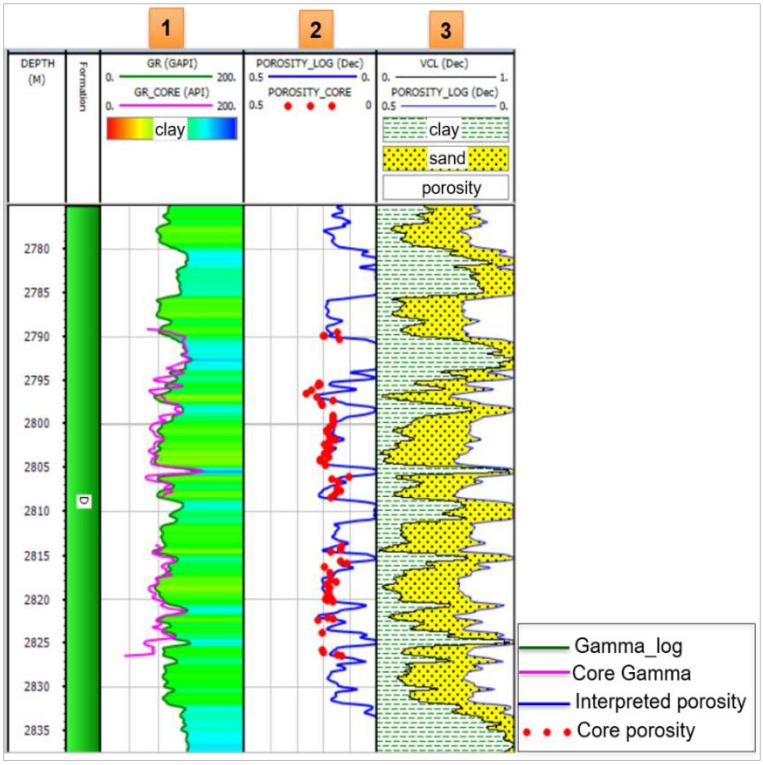


Figure 2b. Example of interpretation defined from core data to validate the well log data: (1) gamma ray value determined by core and well log, (2) Core porosity and interpreted effective porosity from well log, (3) interpreted clay volume and porosity from well log

The lithology classes were further examined in crossplot domains commonly used for petrophysical and rock-physics screening. Figure 3 shows neutron-density and DTC-DTS crossplots superimposed with the main lithology classes. These crossplots indicate that the active D Formation intervals are dominated by sand, shaly sand, and shale. However, the lithology clusters are not completely separated, especially between shaly sand and shale. This overlap suggests that lithology classification cannot rely on a single log response alone and that elastic attributes should be interpreted within a locally calibrated rock-physics framework.

The variables and parameters used in this study have different origins and should therefore be interpreted differently. Measured well logs provide the direct basis for calculating elastic attributes and log-derived saturated moduli. Lithology, shale volume, and porosity classes are interpreted variables derived from petrophysical analysis and constrained by core descriptions, cutting descriptions, mud-log information, and composite-log evidence, where available. The optimized matrix and dry-frame moduli used for RPT construction are not direct laboratory measurements. They are effective rock-physics calibration parameters estimated from the available well-log responses under the selected rock-physics model.

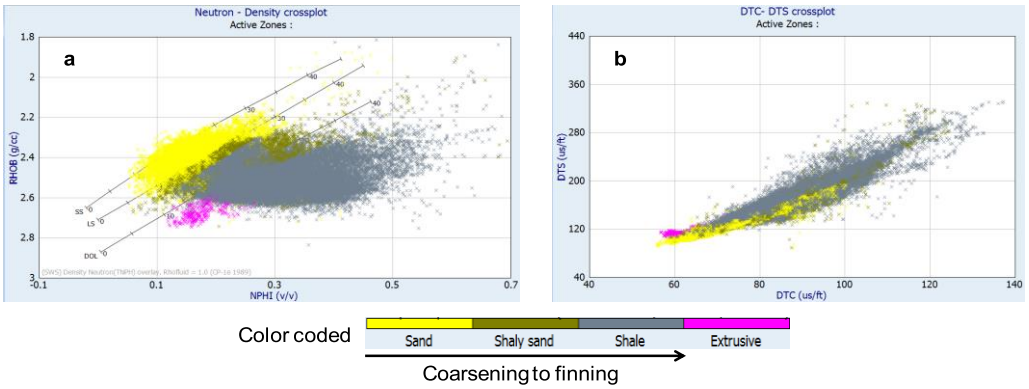


Figure 3. The crossplot of (a) Neutron - Density and (b) DTC-DTS superimposed by main lithologies

Figure 4 provides the main link between the well-log interpretation and the RPT construction. The AI versus Vp/Vs crossplots are color-coded by depth, shale volume, water saturation, and effective porosity. These plots show that the data distribution is controlled not only by lithology but also by depth-related trends, shale content, and variations in saturation and porosity. Sand, shaly sand, and shale samples may partly overlap in the AI-Vp/Vs domain, indicating that a single fixed RPT may not adequately represent the full D Formation interval. This observation provides the basis for constructing interval-dependent RPTs calibrated to the local well-log response and geological context.

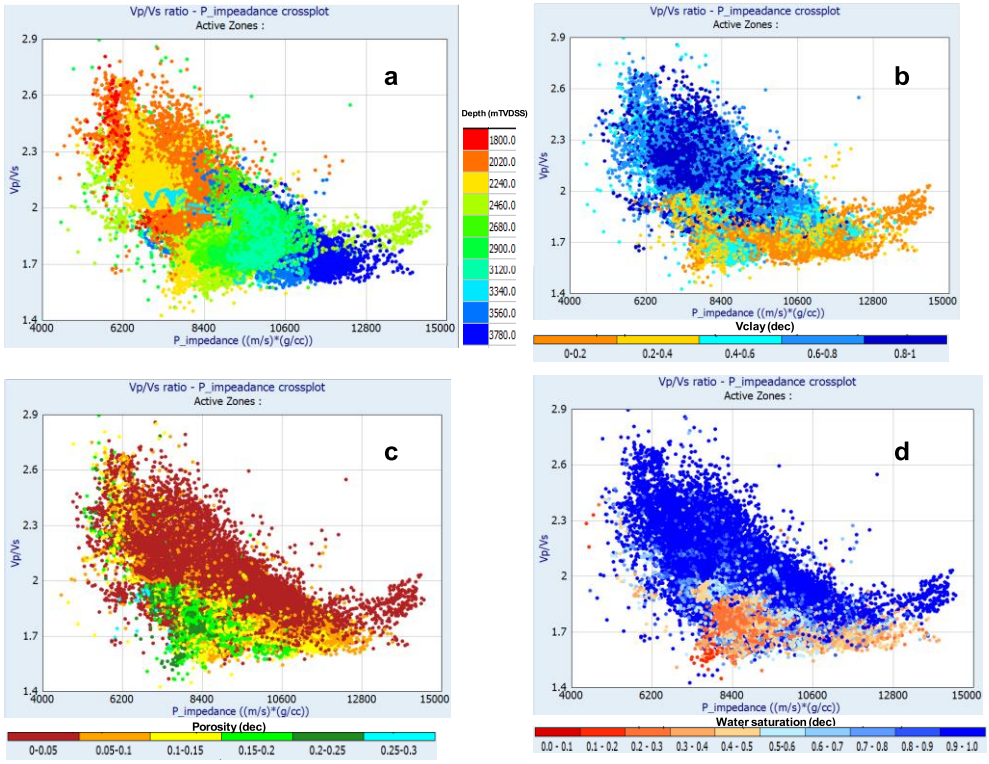


Figure 4. The crossplot between AI and Vp/Vs with (a) color-coded depth, (b) shale volume, (c) saturation, and (d) effective porosity for all wells

Accordingly, the RPT workflow in this study uses the interpreted lithology and petrophysical classes as calibration constraints, while the measured elastic attributes provide the quantitative rock-physics response. The optimized matrix and dry-frame parameters are adjusted to reproduce the logged elastic behavior of each interval. In this way, the RPTs are not constructed as generic templates but as locally calibrated, effective templates that account for observed variation in lithology, shale volume, porosity, and elastic response within the D Formation.

3.2. Conventional rock-physics-template construction

A conventional RPT workflow starts by defining mineral, fluid, and frame properties (Fig. 5). Mineral moduli are estimated for the dominant matrix components and then mixed using bounds or averaging schemes such as Voigt, Reuss, or Voigt-Reuss-Hill averages (Mavko et al., 2009). Fluid properties are estimated from pressure-volume-temperature information and mixed according to the assumed saturation model. The dry-frame moduli are then calculated as a function of porosity using a suitable rock-physics model, such as a soft-sand model. Finally, saturated-rock moduli are calculated using Gassmann fluid substitution, with the shear modulus assumed to be unchanged by fluid substitution under standard Gassmann assumptions.

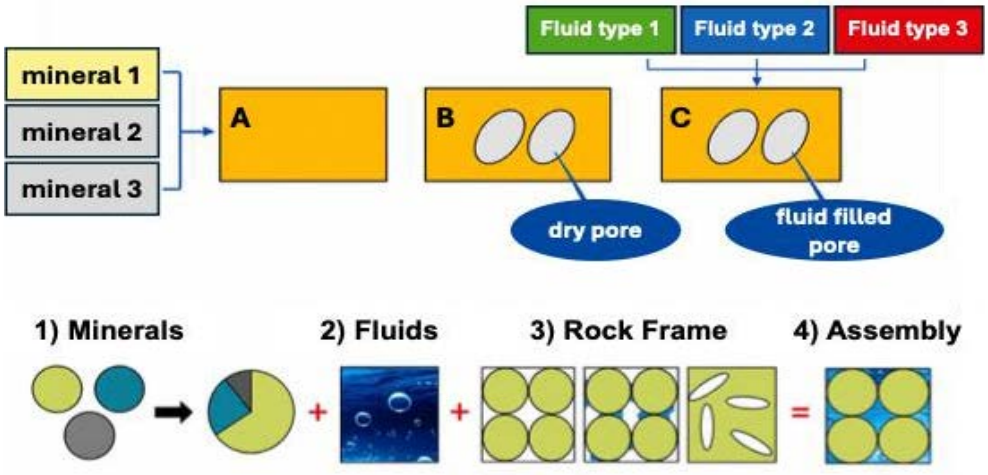


Figure 5. A simple rock model with a solid mineral and a single pore. A- The Frame rock, which is created by some main minerals, B- Frame rock with a single pore (filled by air), and C- Frame rock filled by fluid (adapted from Mavko and Mukerji, 1995) and Rock physics modeling process (Reine, 2017)

The resulting elastic properties are transformed to P-wave velocity, S-wave velocity, density, and impedance. By systematically varying porosity, lithology, and saturation, a family of model curves is created and superimposed on well-log data in the chosen elastic domain. The main limitation of this approach in the present study is that several required parameters, especially dry-frame stiffness and pore-space parameters, are not available from laboratory measurements. A data-driven calibration was therefore adopted.

The proposed workflow estimates effective elastic parameters directly from well-log observations (Fig. 6). For each selected depth window, initial matrix moduli for the dominant lithological end members are defined, including bulk and shear moduli for sand-rich

and shale-rich components. The effective matrix bulk modulus K_m and shear modulus G_m are then obtained by applying a mixing rule based on lithology fraction. These initial values constrain the inversion and reduce the possibility of non-geological solutions.

Table 1 contrasts the proposed workflow with conventional RPT practice, burial-history-guided rock-physics modeling, and recent 3D RPT approaches. Although burial depth affects elastic attributes, the literature well documents this. Our approach introduces a new workflow that calibrates depth-specific effective matrix and dry-frame parameters directly from well-log-derived saturated moduli. These parameters are then used to generate interval-specific templates for the Oligocene D Formation interval under limited laboratory-control conditions.

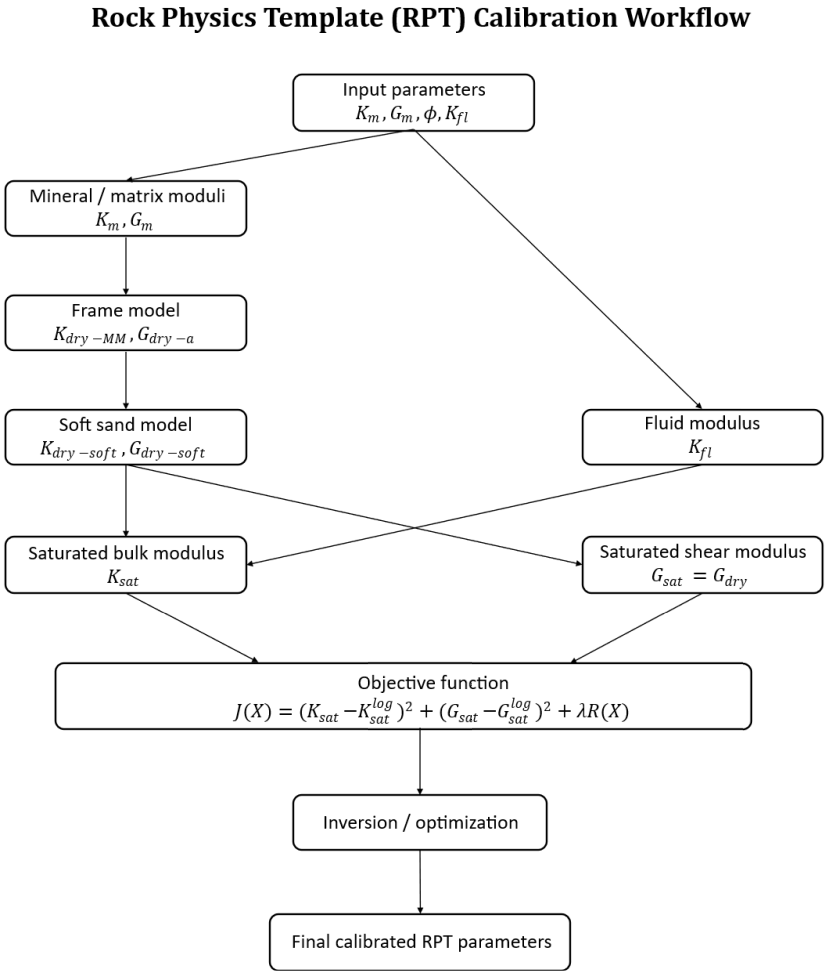


Figure 6. Proposed workflow for rock-physics-based estimation of elastic parameters and construction of the rock physics template (RPT). The procedure starts from mineralogical, petrophysical, and fluid inputs; computes matrix and fluid moduli; estimates dry-frame properties using the soft-sand model; applies Gassmann fluid substitution to obtain saturated moduli; and calibrates model parameters by minimizing the misfit between modeled and logged elastic moduli. More details can be found in the Appendix

Table 1. Comparison of the proposed depth-dependent RPT workflow with related RPT approaches

Approach	Depth/burial treatment	Main limitation
Conventional RPT	Uses fixed mineral-fluid-frame parameters; depth effects are commonly implicit or represented by a single trend	May mix compaction, lithology, and fluid effects in thick heterogeneous intervals
Burial-history-guided RPT	Explicitly uses burial and diagenetic trends to guide rock-physics modeling	Requires reliable burial history and diagenetic constraints that are not always available
3D RPT	Uses multi-dimensional attribute domains; depth may be included as an attribute or constraint	Requires denser calibration data and can be difficult to apply in data-limited settings
Proposed depth-dependent RPT	Calibrates effective matrix and dry-frame parameters separately within depth windows from log-derived Ksat and Gsat	Requires quantitative validation, uncertainty analysis, and more blind wells before full-field application

3.3. Depth-dependent calibration and optimization formulation

Dry-frame moduli are estimated as functions of the effective matrix moduli, porosity, and a frame-stiffness term (see the Appendix for more details). Saturated bulk modulus K_{sat} is calculated using Gassmann substitution, whereas saturated shear modulus G_{sat} is taken as equal to the dry shear modulus under the standard low-frequency Gassmann assumption. Log-derived saturated bulk and shear moduli are computed from measured P-wave velocity, S-wave velocity, and density. The P-wave velocity (m/s) and S-wave velocity (m/s) are inverted from DTC $(\mu s/ft)$ and DTS $(\mu s/ft)$, respectively, with a scale factor of 304800.

After calibration at the well scale, the depth-dependent RPTs are used for two interpretation tasks: (1) lithology discrimination between sand, shaly sand, and shale and (2) preliminary spatial interpolation of optimized elastic parameters away from wells. For the interpolation test, the input consisted of optimized elastic-parameter logs from the wells. Spatial interpolation was performed using external-drift kriging, with depth incorporated as an external drift to account for vertical trends. A three-dimensional spherical variogram model with strong lateral-to-vertical anisotropy was applied, consistent with the stratified nature of the D Formation succession.

For reproducibility, the calibration is formulated as a bounded nonlinear least-squares problem for each well and depth window. The observed saturated bulk and shear moduli are first calculated from logs as $K_{sat} = \rho_b(V_p^2 - 4V_s^2/3)$ and $G_{sat} = \rho_b V_s^2$, where ρ_b is the bulk density and V_P and V_s are P-wave and S-wave, respectively. The modeled saturated moduli are obtained by applying the selected matrix-mixing rule, the dry-frame model, and Gassmann fluid substitution. The parameter vector contains the effective mineral bulk and shear moduli of sand and shale end-members $(K_{sand}, K_{shale}, G_{sand}, G_{shale})$, the Voigt-Reuss mixing parameters (λ_K, λ_G) and the pore space stiffnesses (K_ϕ, G_ϕ), which calibrate the contact moduli at critical porosity. The pore space stiffnesses K_ϕ and G_ϕ are adopted following Russell (2013) as unified calibration parameters that implicitly encode grain contact geometry, cementation degree, and effective pressure. Unlike the original Hertz-Mindlin formulation, which requires independent estimates of coordination number and hydrostatic confining pressure, K_ϕ and G_ϕ reduce the calibration to two physically bounded scalars

that remain approximately constant across the porosity range within each depth window.

The objective function minimized in each depth window is:

$$J(X) = \left(K_{sat} - K_{sat}^{log}\right)^2 + \left(G_{sat} - G_{sat}^{log}\right)^2 + \lambda \cdot R(X)$$

where

- $R(X)$ is a regularization term that penalizes departures from geologically reasonable initial values:

$$R(X) = (X - X_0)^2$$

- The regularisation weight λ was selected empirically to ensure that the regularisation term remains small relative to the data misfit at convergence, thereby stabilizing the inversion without significantly biasing the recovered parameters away from the data-driven solution.

In this study, the Limited-memory Broyden-Fletcher-Goldfarb-Shanno with Bounds (L-BFGS-B) method is used as the optimization algorithm. This algorithm is suitable for large-scale optimization problems with simple bound constraints and has been widely used for limited-memory quasi-Newton optimization where full Hessian estimation is not practical (Byrd et al., 1995; Zhu et al., 1997). The numerical bounds, lambda value, maximum number of iterations, and convergence tolerance are described in Table 2.

Table 2. Reproducibility information required for the optimization

Item	Description	Value to report
Optimized variables	Effective mineral bulk and shear moduli of sand and shale; the Voigt-Reuss mixing parameters and the pore space stiffnesses for each depth window	$K_{sand}, K_{shale}, G_{sand}, G_{shale}, \lambda_K, \lambda_G, K_\phi, G_\phi$
Lower/upper bounds	Physical or empirical bounds for each optimized parameter	K_{sand} – (25, 100) G_{sand} – (5, 60) K_{shale} – (0, 60) G_{shale} – (0, 15) λ_K – (0, 1) K_ϕ – (0, 20) λ_G – (0, 1) G_ϕ – (0, 20)
Regularization weight lambda	Weight balancing data misfit and deviation from initial parameters	0.08
Weights w_K and w_G	Weights for bulk- and shear-modulus mismatch terms	1:1
Maximum iterations	Maximum L-BFGS-B iterations per depth window	maxiter = 15000
Convergence criterion	Function tolerance, gradient tolerance or parameter tolerance	ftol = 2.22e-9, gtol = 1e-5

3.4. Quantitative validation strategy

The optimization and prediction performance are evaluated using both regression metrics for elastic attributes and classification metrics for lithology prediction. For elastic attributes (such as Vp, Vs, AI, and Vp/Vs), the metrics are Root Mean Square Error (RMSE), Mean Absolute Error (MAE), coefficient of determination (R^2), and Pearson correlation coefficient. RMSE and MAE were used to measure the absolute prediction error, with RMSE giving greater weight to larger errors and MAE providing a more direct measure of the average absolute deviation (Chai and Draxler, 2014). R^2 was used to evaluate the proportion of observed variance explained by the model. In contrast, the Pearson correlation coefficient was used to assess the strength of the linear association between the measured and modeled elastic attributes (Chicco et al., 2021).

For lithology classification, the generalized RPT, overall accuracy, and macro-averaged F1-score were used. The F1-score was used as a combined measure of precision and recall, particularly useful when class proportions are not perfectly balanced (Sokolova and Lapalme, 2009; Powers, 2011).

Table 3. Recommended validation metrics for elastic-attribute prediction and RPT-based lithology classification (N is the number of samples)

Quantity	Metric	Formula or definition
Elastic prediction	RMSE	$\sqrt{\sum(y_{obs} - y_{mod})^2/N}$
Elastic prediction	MAE	$\sum\|y_{obs} - y_{mod}\|/N$
Elastic prediction	R2	$1 - \frac{(y_{obs} - y_{mod})^2}{(y_{osb} - mean(y_{obs}))\text{^}2}$
Elastic prediction	Pearson r	linear correlation between observed and modeled values
Lithology prediction	Accuracy	number of correct labels / total samples
Lithology prediction	Macro F1-score	mean F1-score across sand, shaly sand and shale classes

4. Results

The calibration workflow was first applied to representative wells and then extended to the full well set. The initial moduli constraints were obtained from crossplots of moduli, porosity and shale volume, allowing matrix values to be approximated under low-porosity or clay-free conditions (Fig. 7). For sandstone, the initial estimates are derived from the extrapolation of bulk and shear modulus trends toward the zero-porosity end member rather than from direct laboratory tests. These constraints help stabilize the nonlinear optimization and prevent the selection of unrealistic elastic parameters.

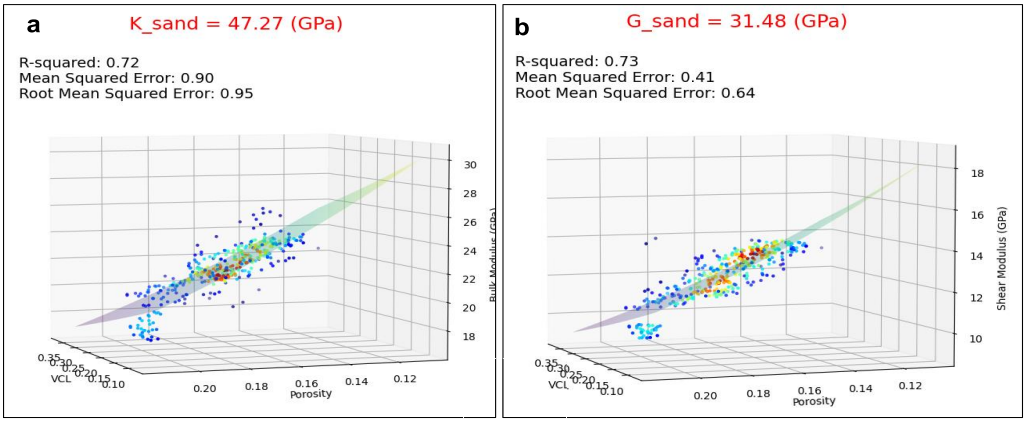


Figure 7. The estimation of initial values of modulus is selected by approximation K_{sand} (a) and G_{sand} (b) with no porosity. Three-dimensional representations of model constraints for the data parameters for the bulk and shear modulus of sandstone

The elastic moduli optimization was first performed over the entire D Formation interval at well X1, and the results are presented in Fig. 8.

The back-calculated P- and S-wave velocities are generally consistent with the measured well-log velocities. The agreement is evident in both the depth-domain comparison and the measured-versus-calculated velocity crossplots (Fig. 8).

For Vp, the RMSE and MAE are 177.95 m/s and 146.1 m/s, respectively, representing approximately 4–5% of the measured Vp range. For Vs, the RMSE and MAE are 138.78 m/s and 118.02 m/s, corresponding to approximately 5–6% of the measured Vs range. Although the coefficients of determination (R^2 = 0.25 for Vp and R^2 = 0.14 for Vs) and Pearson correlation coefficients (r = 0.63 and r = 0.49,

respectively) are relatively modest, this is expected given that the optimized bulk and shear moduli are intended to represent average elastic properties for RPT construction rather than to reproduce point-by-point velocity variations. This result indicates that the optimized elastic parameters capture the main elastic behavior of the intervals studied and can be used to generate depth-dependent templates.

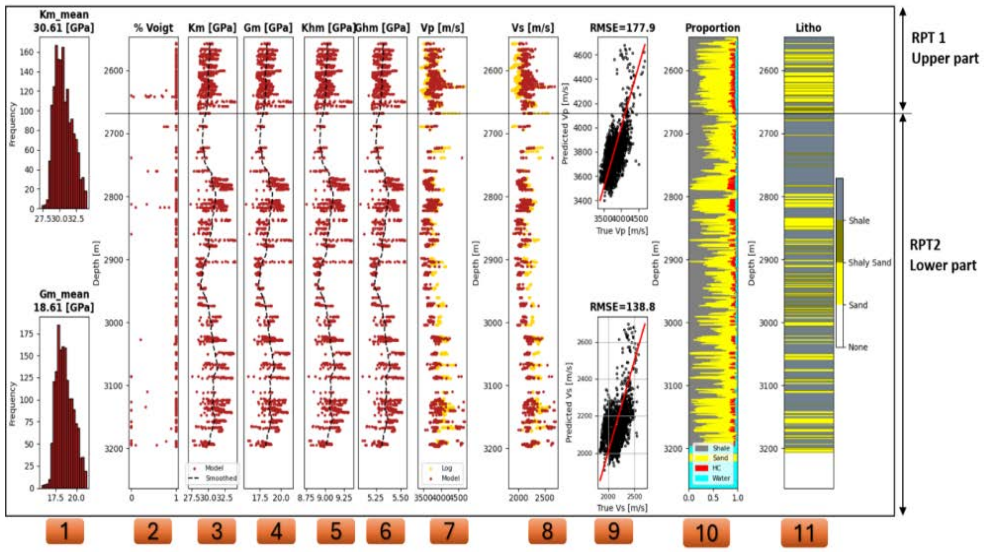


Figure 8. Results of optimized elastic parameters at well X1 (optimized over the whole interval). (1): Histogram of predicted Km and Gm of sand, (2): The predicted mixing matrix, (3): The predicted Km of sand, (4): The predicted Gm of sand, (5): The predicted Km of sand at critical porosity, (6): The predicted Gm of sand at critical porosity, (7): The comparison of measured (red line) and back-calculated (yellow line) P-wave velocity, (8): The comparison of measured (red line) and back-calculated (yellow line) S-wave velocity, (9): The cross-plot of measured and back-calculated wave velocity, (10) proportion of various lithology content, (11) Lithology content

However, a closer inspection of the optimized parameter logs reveals systematic vertical variation in $K_m, G_m, K_{dry}, G_{dry}$ throughout the interval (Fig. 8, tracks 3–6), suggesting that a single average parameter set is insufficient to characterize the full interval. At well X1, D Formation consists of interbedded sandstones and shales and can be divided into at least two elastic intervals. The upper interval from approximately 2547–2669 mTVDSS (2792–2970 mMD) is dominated by a more blocky sand-prone package, whereas the lower interval from approximately 2669–3198 mTVDSS (2970–3669 mMD) contains more interbedded sand-shale facies. Accordingly, the optimization was subsequently performed separately for each sub-interval to better capture the distinct elastic characteristics, as discussed in the following section.

When the interval is subdivided into two smaller rock-physics template zones, the model performance improves substantially. This improvement is evidenced by the closer agreement between the modeled Vp and Vs and the measured logs, as shown in Fig. 9, where only minor discrepancies are observed between the black and orange curves. In RPT 1-upper part, Vp gives the best overall result, with the lowest Vp error among all

intervals: RMSE = 89.22, MAE = 72.76, R^2 = 0.80, and Pearson r = 0.91. This indicates a strong linear relationship and good predictive capability. Vs in the same interval also improves compared with the full formation RPT, with RMSE = 74.79, MAE = 61.22, R^2 = 0.63, and Pearson r = 0.82.

For RPT 2 - lower part, the results are better than those for the entire formation but generally slightly weaker than those for RPT 1. Vp achieves RMSE = 101.37, MAE = 75.15, R^2 = 0.71, and Pearson r = 0.87, showing a good but less optimal fit than in the upper interval. Vs gives the lowest absolute error overall, with RMSE = 71.02 and MAE = 50.61, but its R^2 of 0.60 and Pearson r of 0.81 indicate that the correlation strength is still slightly lower than that of Vp.

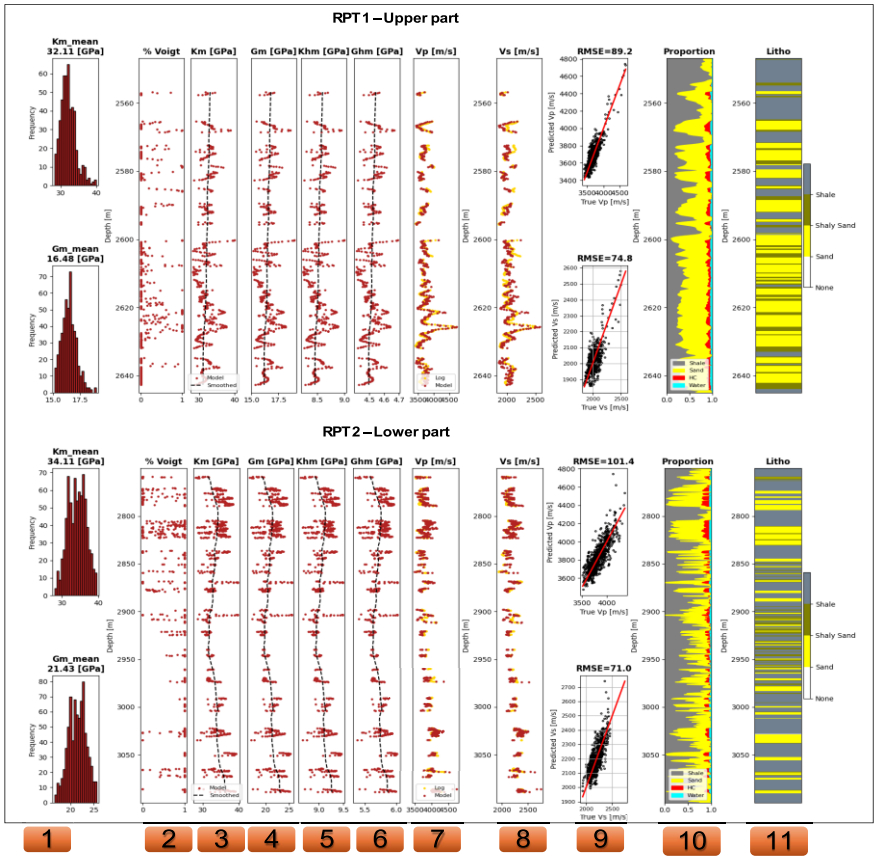


Figure 9. Results of optimized elastic parameters at X1 (optimized for two separated intervals). (1): Histogram of predicted Km and Gm of sand, (2): The predicted mixing matrix, (3): The predicted Km of sand, (4): The predicted Gm of sand, (5): The predicted Km of sand at critical porosity, (6): The predicted Gm of sand at critical porosity, (7): The comparison of measured (red line) and back-calculated (yellow line) P-wave velocity, (8): The comparison of measured (red line) and back-calculated (yellow line) S-wave velocity, (9): The cross-plot of measured and back-calculated wave velocity, (10) proportion of various lithology content, (11) Lithology content

Table 4 summarizes regression metrics for both a single RPT and the interval-specific RPTs. These values are calculated at the original log-sampling resolution for each well

and depth window after removing bad-hole intervals and samples with missing DTC, DTS, or RHOB values.

RPTs constructed for the two depth intervals at Well X1 show distinct positions and trends in the AI versus Vp/Vs domain. (Fig. 10). The measured data form a broad triangular cloud, with reservoir-quality samples concentrated mainly at moderate to high P-impedance and relatively low Vp/Vs. Shale-rich samples occupy higher Vp/Vs values, whereas cleaner sand-prone samples tend to plot at lower Vp/Vs. The two templates are therefore not interchangeable: RPT1 is appropriate for the shallower interval, whereas RPT2 better represents the deeper interval.

Table 4. Quantitative goodness-of-fit statistics for measured versus modeled elastic attributes at well X1

Well/depth window	Attribute	RMSE	MAE	R2	Pearson r
X1 Entire D Formation	Vp	177.95	146.10	0.25	0.63
	Vs	138.78	118.02	0.14	0.49
X1 RPT 1 - upper part	Vp	89.22	72.76	0.80	0.91
	Vs	74.79	61.22	0.63	0.82
X1 RPT 2 - lower part	Vp	101.37	75.15	0.71	0.87
	Vs	71.02	50.61	0.60	0.81

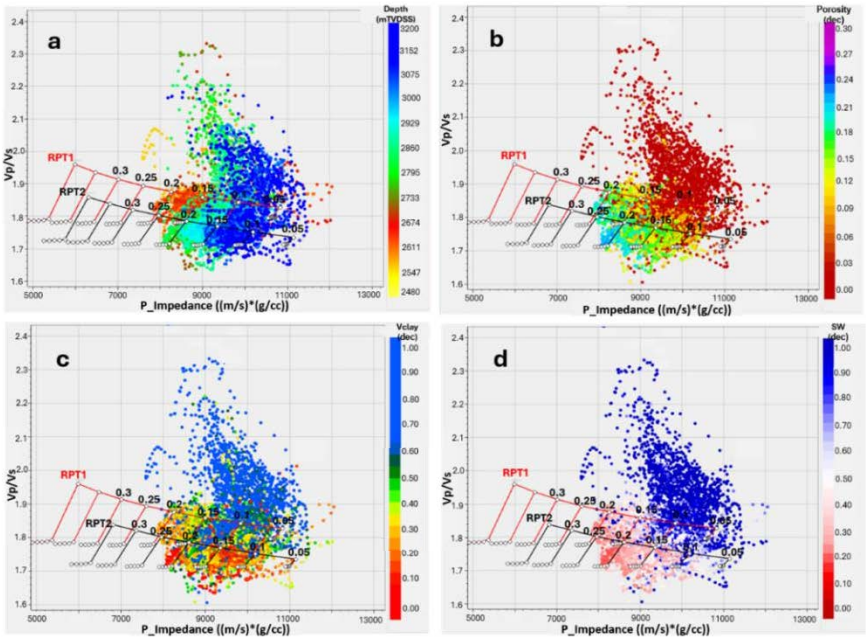


Figure 10. Crossplot of AI vs. Vp/Vs with superimposed two RPTs for the interval (well X1), color-coded (a) Depth, (b) Porosity, (c) Vclay, (d) Water saturation

The depth-colored crossplots demonstrate that burial depth shifts the elastic background. Deeper samples generally move toward higher impedance as compaction increases rock-frame stiffness. This effect causes the same lithology to occupy different positions within the elastic domain at different depths. Therefore, using a single RPT across the entire interval may conflate lithological and compaction effects, leading to misleading sand-shale boundaries.

Porosity and water saturation also influence the elastic response. Higher-porosity samples generally correspond to lower impedance and lower-to-moderate Vp/Vs,

whereas tighter intervals tend toward higher impedance. The saturation panels show that high water saturation is associated with higher Vp/Vs. In comparison, lower water saturation tends to move the response toward lower Vp/Vs at a given impedance. These trends are consistent with the expected fluid- and pore-volume-related effects in the RPT framework and justify the use of separate depth-calibrated templates.

Figure 11 compares lithology predictions from depth-specific RPTs with those from a single generalized template. When RPT2 is applied to the deeper interval, the predicted sand intervals are more consistent with the well-log interpretation. However, using RPT2 for the shallower interval overestimates shale-prone facies. Conversely, RPT1 performs well in the shallower interval but is less suitable for the deeper part of the well. The single-template case produces mismatches in the upper interval, underscoring the risk of applying a single template to the full D Formation section.

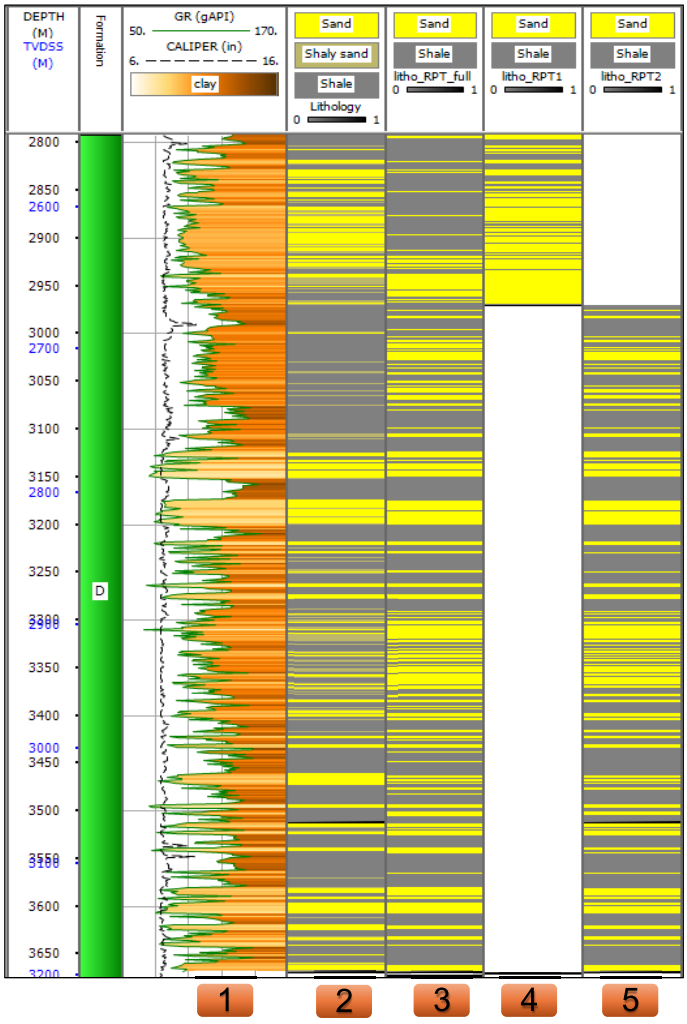


Figure 11. Lithology defined by using various RPTs scenarios with (1) - Gamma Ray (gAPI) (2) - True lithology content of the well, (3) - Lithology predicted by using one RPT for whole interval, (4) - Lithology defined by optimized RPT 1 in the upper part and (5) - Lithology defined by optimized RPT 2 in the lower part

For a consistent comparison, the prediction results from the whole-well RPT were also divided into the same two depth intervals used for the interval-specific RPTs. Overall, the interval-specific RPTs show improved predictive performance compared with the single whole-well RPT. This improvement is reflected by higher classification metrics, including accuracy, precision, recall, and F1-score, particularly in the interval where the lithological variability is more pronounced. In the upper interval, the whole-interval RPT performs relatively poorly, with weighted precision, recall, and F1-score of 0.59, 0.58, and 0.48, respectively. After applying the optimized RPT1 for the upper interval, these metrics increase to 0.70, 0.71 and 0.71, indicating a substantial reduction in lithology misclassification. In the lower interval, the whole-interval RPT already provides moderate performance, with weighted precision, recall and F1-score of 0.76, 0.77 and 0.78 (Table 5). However, the optimized RPT2 further improves the results to 0.80, 0.81 and 0.80, respectively. These results demonstrate that depth-dependent RPT calibration provides a more reliable lithology prediction than a single generalized template, especially where the elastic response varies significantly with depth. The whole-well RPT provides a more generalized prediction, but its performance decreases when applied to intervals with distinct elastic or petrophysical characteristics. This suggests that a single global RPT may not fully capture depth-dependent variations in rock physics behavior.

Table 5. Comparison of lithology prediction metrics obtained from different rock physics templates (RPTs). The whole-well RPT was evaluated separately over two depth intervals to allow direct comparison with interval-specific RPTs. The results indicate that interval-specific RPTs generally achieve better classification performance, suggesting that local calibration improves lithology prediction when rock physics behavior varies with depth.

Lithology predicted by using one RPT for the whole interval, metric for the upper part				
	Predicted sand	Predicted shale		
Actual sand	244	513		
Actual shale	63	348		
	precision	**recall**	**f1-score**	**number of samples**
weighted avg	0.59	0.58	0.48	1169
Lithology predicted by using one RPT for the whole interval, metric for the lower part				
	Predicted sand	Predicted shale		
Actual sand	1149	359		
Actual shale	633	2442		
	precision	**recall**	**f1-score**	**number of samples**
weighted avg	0.76	0.77	0.78	4584
RPT1 - upper part				
	Predicted sand	Predicted shale		
Actual sand	629	128		
Actual shale	206	205		
	precision	**recall**	**f1-score**	**number of samples**
weighted avg	0.7	0.71	0.71	1169
RPT2 - lower part				
	Predicted sand	Predicted shale		
Actual sand	1073	435		
Actual shale	495	2581		
	precision	**recall**	**f1-score**	**number of samples**
weighted avg	0.8	0.81	0.8	4584

In contrast, the RPTs constructed for individual intervals better represent the local relationship between elastic properties and lithology. As a result, they reduce lithology misclassification and provide more reliable predictions within their respective calibration ranges. The comparison indicates that interval-based RPT calibration is preferable when the well section contains significant changes in lithology, compaction trend, fluid effect, or elastic response.

These results demonstrate that lithology prediction using RPTs is sensitive to the calibration scale. While a whole-well RPT is useful for obtaining a broad prediction trend, dividing the well into geologically or petrophysically consistent intervals can enhance prediction accuracy and improve the robustness of lithology classification.

The crossplots compare RPT-predicted porosity with well-log-derived porosity across two depth intervals (Fig. 12). In both cases, the data show a clear positive relationship, and the mean well-log porosity values closely follow the 1:1 reference line, indicating that the RPT models reproduce the general porosity trend observed in the wells. The left plot shows strong agreement between predicted and measured porosity, with an RMSE of 0.0046 and an R^2 of 0.980. This suggests that, within this depth interval, the RPT-derived porosity accurately predicts the well-log porosity, with only minor deviations from the 1:1 line. The right plot also shows a consistent positive correlation, although the agreement is weaker, with RMSE = 0.0108 and R^2 = 0.834. The larger scatter and error bars indicate higher uncertainty at this depth interval, possibly reflecting greater lithological variability, reduced sensitivity of the RPT model, or local differences between the modeled rock-physics response and the actual well-log measurements. Overall, the results demonstrate that the RPT model provides reliable porosity predictions, with better performance in the first depth interval and moderately lower, yet still acceptable, performance in the second interval.

A common observation across many boreholes is that the elastic properties of sand samples vary considerably, even when the RPTs are subdivided by depth. Well X2 was used to assess the influence of shale volume on elastic response. This well contains water-bearing sands in the D Formation.

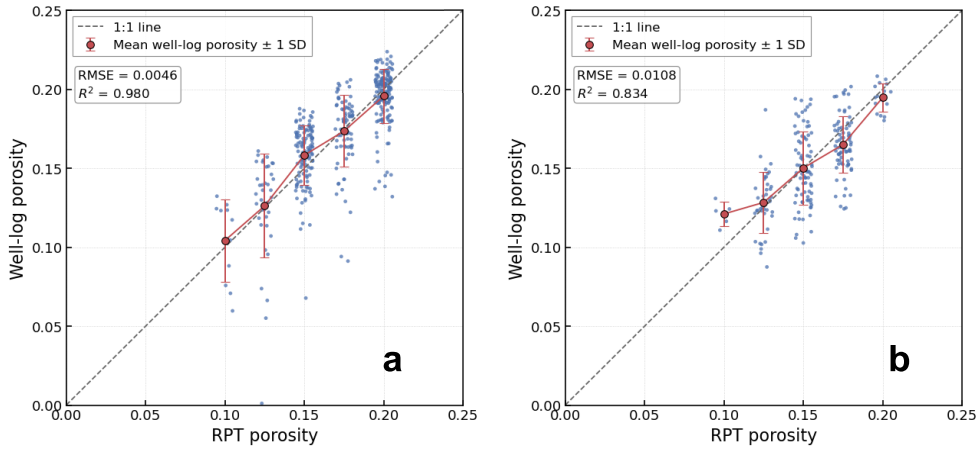


Figure 12. Crossplots showing the validation of RPT-predicted effective porosity for sandstones against well-log-derived porosity at two depth intervals, (a) and (b) respectively for upper and below intervals

In Fig. 13, a positive linear relationship is observed between Vp/Vs and clay volume (Vp/Vs = 1.655 + 0.345·Vclay, R^2 = 0.71), indicating that clay content exerts a significant and continuous influence on Vp/Vs across the full lithofacies spectrum, from clean sand to shale. Complementarily, P-impedance exhibits a negative linear trend with clay volume (AI = 12135–2251·Vclay, R^2 = 0.50), reflecting the lower acoustic stiffness of clay-rich lithologies relative to clean sand. However, sand samples with different Vclay values exhibit distinct Vp/Vs ratios and P-impedance (AI), despite belonging to the same broad lithological class (Fig. 13). For instance, sand-prone samples show Vp/Vs values ranging from 1.6 to 1.9 and P-impedance values of approximately 9,000–14,000 GPa. These results confirm that shale volume should be considered when constructing or selecting RPTs for lithology prediction.

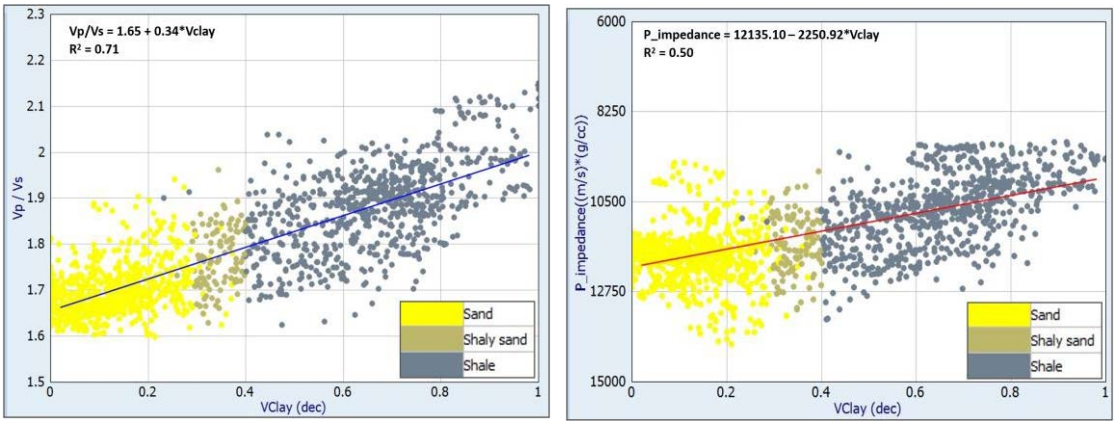


Figure 13. Crossplot of Vp/Vs ratio and P-impedance (AI) versus clay volume (Vclay) for the calibration dataset, colored by lithofacies

Figure 14 compares an interval-averaged RPT with a template that explicitly accounts for Vclay variation. The Vclay-sensitive template better represents the spread of data in the AI versus Vp/Vs domain and reduces the risk of interpreting shaly sand as shale. For hydrocarbon-bearing wells, the interpretation becomes more complex because gas or oil saturation may reduce Vp/Vs and overlap with lithological effects. Incorporating RPTs with variable Vclay content improves the ability to distinguish fluid-related changes from lithology-related changes.

Depth-trend-constrained spatial interpolation (Drift Kriging) of the optimized elastic parameters was implemented to predict RPT templates at undrilled locations. Input data comprised well-optimized elastic-parameter sets from 15 calibration wells (Fig. 1). Directional experimental variograms were computed along X, Y, and Z directions and fitted with theoretical models selected by minimum RMSE (Fig. 15). A spherical model with depth (Z) as external drift best described the horizontal spatial continuity, with fitted ranges of ~50 km (major) and ~40 km (minor) and a horizontal-to-vertical anisotropy ratio of ~40–50 (Table 6). The interpolated templates were validated against three blind-test wells located in spatially distinct areas of the field (Fig. 16). Performance was quantified by comparing RPT-based lithofacies predictions directly against well-log lithology. The results demonstrate that the interpolated templates can reliably discriminate reservoir sand from non-reservoir facies across different structural settings within the field.

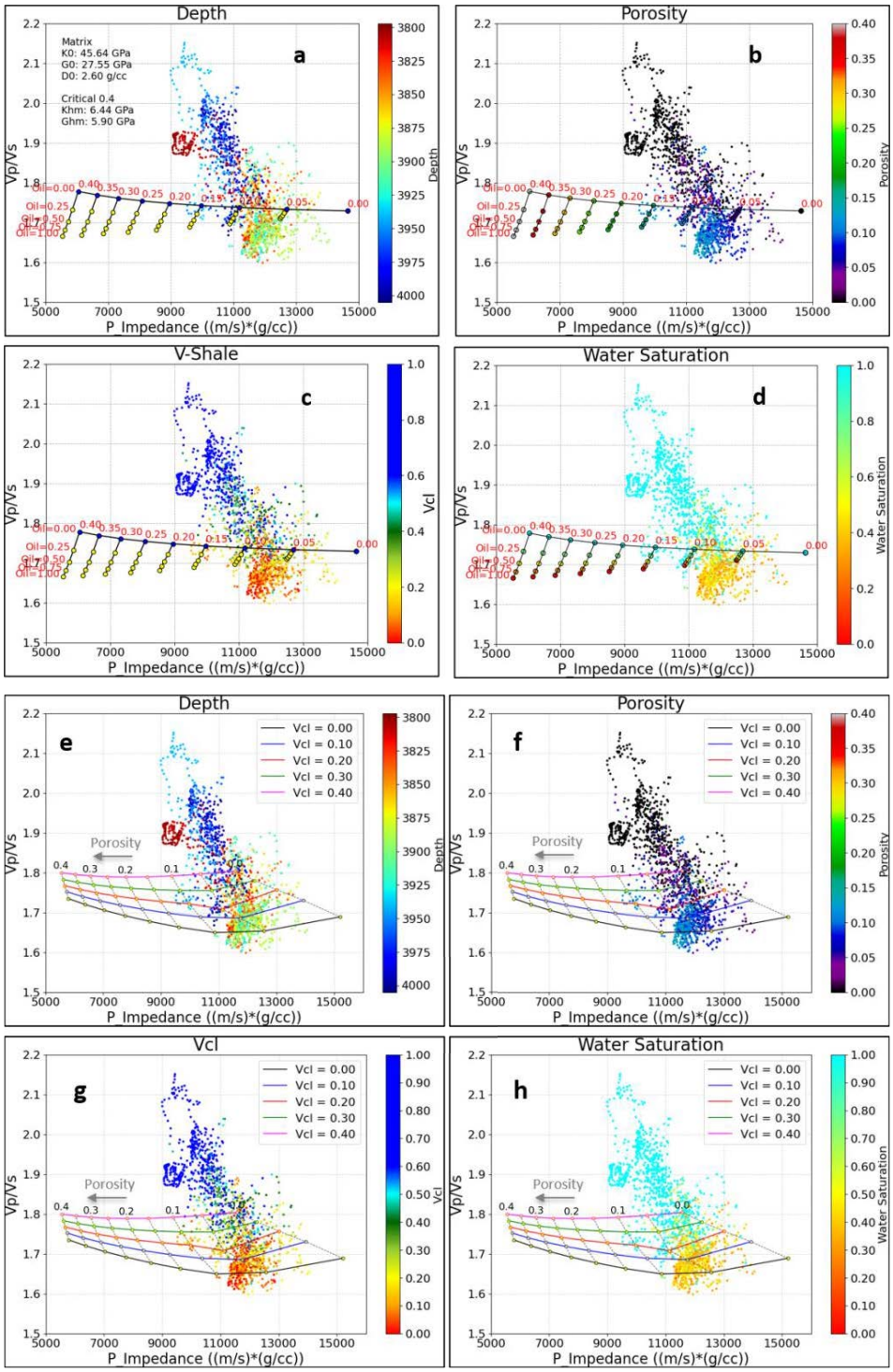


Figure 14. Results of optimized elastic parameters at well X2: Upper- RPTs by averaging for interval-color-coded (a) depth level, (b) Porosity, (c) Vclay, (d) Water saturation; below- RPT with Vclay variation- color-coded (e) depth level, (f) Porosity, (g) Vclay, (h) Water saturation

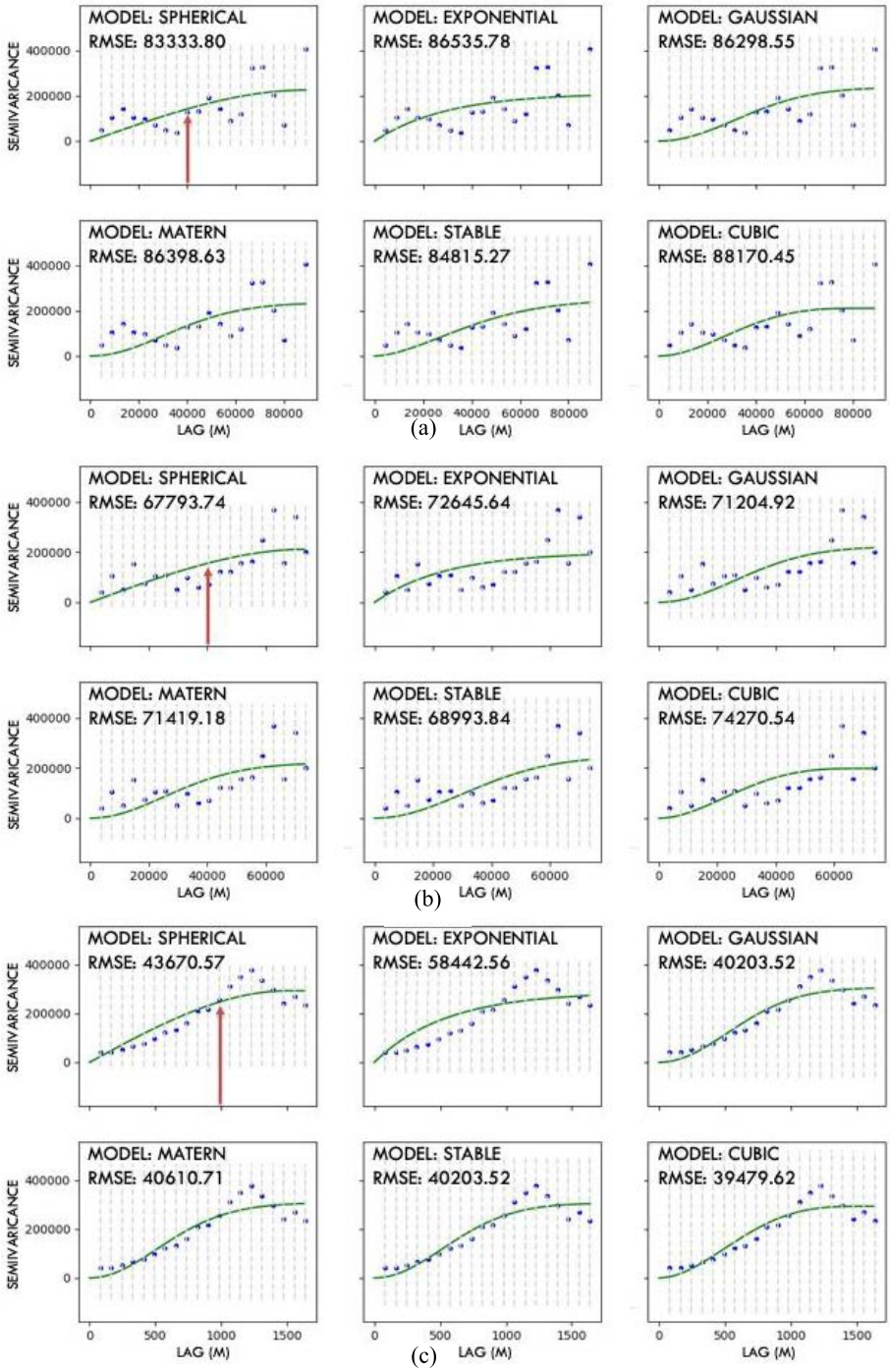


Figure 15. Directional experimental variograms of Vp along (a) X, (b) Y, and (c) vertical direction Z, with six fitted theoretical models. RMSE values indicate the Spherical model best describes horizontal spatial variability, while the Cubic model provides the best fit vertically. Fitted ranges are ~40,000–50,000 m (horizontal) and ~1,000 m (vertical)

Table 6. Summary of Drift Kriging model parameters used for spatial interpolation of the optimized RPT elastic parameters

Parameter	Recommended reporting item	Value to report
Experimental variogram	Number of lags, lag spacing and directional search tolerance	Directional: X, Y (lag max ~90 km, ~70 km), Z (lag max ~1,600 m); Spherical fit selected by overall minimum RMSE (Fig. 15)
Fitted variogram	Model type, nugget, sill and range	Spherical; nugget=0; sill≈200,000 matheron; range: X≈50 km, Y≈40 km, Z≈1,000 m
Anisotropy	Major/minor/vertical ranges or anisotropy ratio	Major (X): 50,000 m; Minor (Y): 40,000 m; Vertical (Z): 1,000 m; H/V ratio ≈ 40–50
External drift	Depth or structural variable used as drift	Depth (Z)
Blind-test status	Interpolation inside well-control area or extrapolation	Interpolation inside well-control area

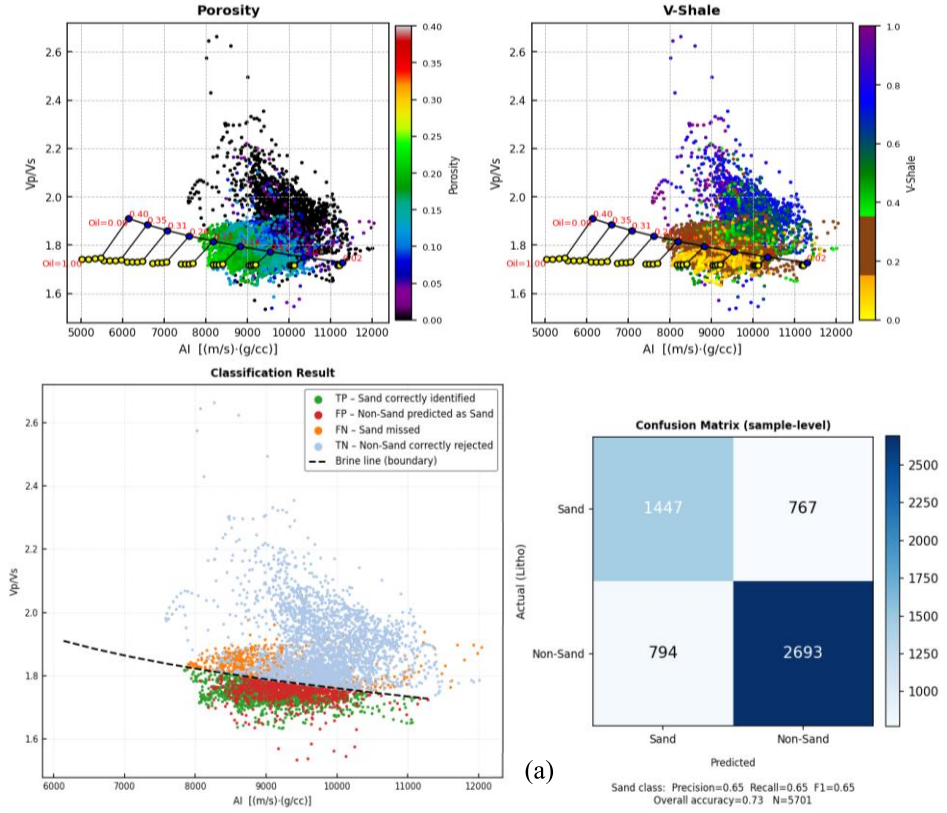


Figure 16. RPT-based lithofacies classification results for three blind-test wells: (a) B1, (b) B2, and (c) B3. For each well, upper panels show RPT crossplots (AI vs. Vp/Vs) colored by porosity and Vclay overlain by the soft-sand template grid; the lower-left panel shows classification outcomes (TP/FP/FN/TN) relative to the Sw = 1 brine line used as the decision boundary; the lower-right panel shows the confusion matrix with precision, recall, and F1-score for the sand class

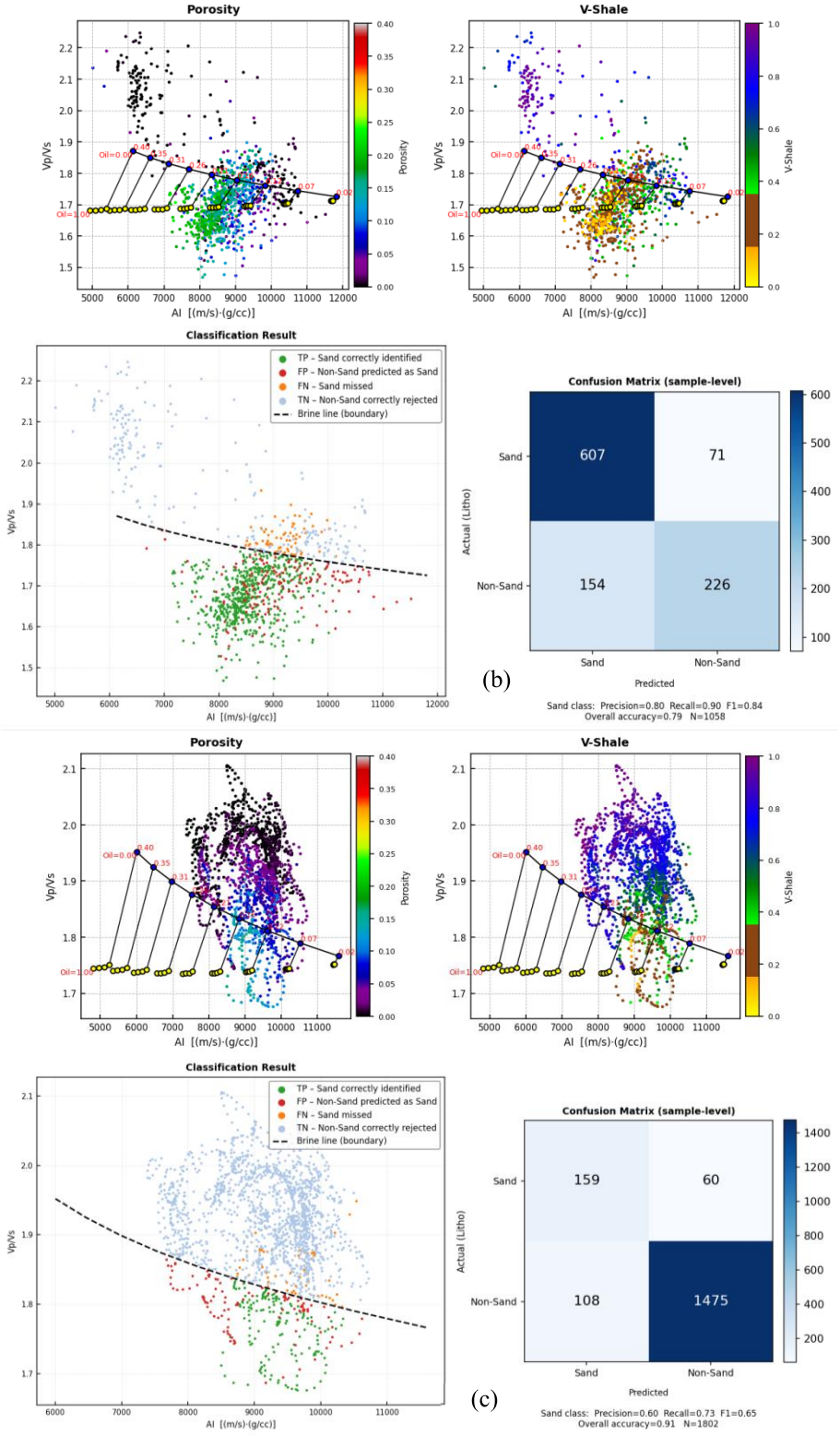


Figure 16. Cont.

Across the three blind-test wells, each located in a spatially distinct area of the study area, F1 scores of 0.65–0.84 and overall accuracies of 0.73–0.91 indicate consistent moderate classification performance. The variation between wells reflects local differences in elastic parameters and the interpolation distance relative to the calibration wells. Importantly, the objective of this workflow is not point-by-point lithofacies prediction but the construction of a spatially continuous low-frequency elastic model for seismic inversion, where the core requirement is the reproduction of broad facies distribution trends and elastic contrasts at the inversion grid scale (typically tens of meters). At that scale, the achieved F1 range of 0.65–0.84 is encouraging. The RPT framework correctly captures the dominant elastic character of each zone. It reproduces the large-scale sand–shale distribution with sufficient reliability to serve as a low-frequency model input. These results demonstrate that depth-dependent Drift Kriging of RPT parameters is a tractable, geologically consistent approach for interpolating elastic properties across the study area.

5. Discussions

The results demonstrate that depth dependence is a first-order control on the elastic expression of D Formation. The observed shifts of the RPTs in the AI versus Vp/Vs domain are likely controlled by a combination of factors, including depth-related compaction, burial-related stiffening, cementation, pore-structure variation, pressure conditions, shale content, diagenetic modification, fluid saturation, and possible anisotropy. Therefore, these shifts should not be attributed solely to compaction. Instead, they indicate that the elastic background varies across the studied interval and that a single fixed template cannot reliably represent lithology classes. This finding is consistent with previous rock-physics studies showing that depositional and burial history affect the relationship between reservoir properties and elastic attributes.

Shale volume introduces an additional source of ambiguity. Samples classified as sand may have different elastic responses when the clay fraction changes. In the studied wells, increasing Vclay generally increases Vp/Vs and moves samples toward the shale-prone part of the crossplot. If this effect is ignored, shaly sand may be misclassified as shale, or cleaner sand may be overlooked in intervals where compaction has shifted to the elastic background.

5.1. Contextualization within Vietnamese and international rock-physics studies

International rock-physics studies have shown that a single rock-physics template cannot be used universally for all sedimentary intervals (Avseth et al., 2001, 2014; Fawad et al., 2020). Several factors, including lithology, shale volume, mineral composition, porosity, pore structure, cementation, compaction, fluid content, pressure, burial depth and diagenetic history, control the elastic response of sediments. As these factors vary between formations and even within subintervals of the same stratigraphic succession, the parameters used to construct RPTs must be locally calibrated and, where necessary, updated for different geological intervals. This is particularly important in heterogeneous clastic successions, where interbedded sand, siltstone, and shale may exhibit overlapping elastic responses, and where shale content or burial-related compaction can obscure the effects of lithology and fluid.

In this context, the D Formation case differs from many conventional RPT applications, where a template is commonly constructed for a specific reservoir body, a single sand unit, or a selected target interval. Instead of applying a single fixed RPT to the

entire sedimentary succession, the present workflow builds and calibrates multiple RPTs for different stratigraphic subintervals within the D Formation. This approach allows rock-physics parameters to vary with depth and geological setting, thereby better accounting for changes in compaction, lithological composition, shale content, and effective frame properties. The results demonstrate that interval-dependent RPTs provide a more realistic framework for interpreting porosity and lithology in a heterogeneous clastic system than a single generalized template.

In Vietnam, published RPT studies remain relatively limited. Existing studies in the Nam Con Son Basin have emphasized the need to adapt rock-physics parameters to field data rather than rely on default values (Giao et al., 2021). These works have shown that parameters such as mineral composition, critical porosity, elastic bounds, dry-frame moduli, and other rock-physics inputs can significantly affect the construction and interpretation of RPTs. However, most available Vietnamese examples have focused on a particular reservoir sand or gas-bearing turbidite sand, rather than developing a set of multiple depth- or interval-dependent RPTs for a broader sedimentary succession.

Therefore, the main contribution of the present D Formation study is not the introduction of a new theoretical rock-physics model, but the development of a practical calibration workflow for data-limited clastic sediments in the Cuu Long Basin. By estimating effective matrix and dry-frame parameters from well logs, calibrating them against available lithological and petrophysical information, and updating the templates for different stratigraphic intervals, the workflow reduces reliance on fixed default parameters. It provides a bridge between well-scale rock-physics interpretation and seismic-scale reservoir characterization. This approach is especially useful for Vietnamese rift-related clastic basins, where sedimentary facies, burial depth, structural relief and data availability may vary significantly from one interval to another.

5.2. Applicability and limitations of the Gassmann assumption

The use of Gassmann fluid substitution should be considered an effective low-frequency approximation rather than an exact description of all D Formation facies. Gassmann theory assumes a connected pore system, a homogeneous and isotropic rock frame, no chemical interaction between the rock and the fluid, and pressure equilibration at the seismic frequency scale. These assumptions may be challenged in shale-rich and shaly-sand intervals, where clay distribution, lamination, pore-shape variability, anisotropy, and partial saturation can produce dispersion or patchy-saturation effects (De Jonge-Anderson et al., 2021). Consequently, the calibrated parameters in this study are interpreted as effective parameters conditioned by the selected rock-physics model and the available logs. The uncertainty is expected to be larger in laminated shale and shaly-sand intervals than in cleaner sandstone intervals.

6. Conclusions

This study proposes a data-driven workflow for constructing depth-dependent rock-physics templates for the D Formation in the Cuu Long Basin. Well-log data show that the elastic response of D Formation varies systematically with depth. A single whole-interval RPT provides a less accurate representation than interval-specific templates because depth-related elastic variations shift the AI-Vp/Vs trends. The optimized matrix and dry-frame elastic parameters reproduce the main trends in P-wave and S-wave velocities observed in the wells, indicating that well-log-based calibration can yield practical RPT parameters when laboratory measurements are unavailable. Crucially,

blind-test validation across three spatially distinct wells confirmed the strong predictive capability and regional applicability of the proposed model, achieving high overall classification accuracies of 0.73–0.91 and F1-scores of 0.65–0.84. Furthermore, as shale volume significantly affects elastic response, it should be integrated when applying RPTs to shaly sand and shale-prone intervals, especially where lithology and fluid effects overlap.

The 3D spatial interpolation in this study is intended as a preliminary experimental analysis rather than a final geological or reservoir property model. Depth was used as the main external drift variable to capture the first-order compaction-related trend in the available well data.

Regional investigations of the Cuu Long Basin indicate that its Cenozoic evolution was characterized by multiple episodes of extension, compression, thermal subsidence, and subsequent tectonic stabilization (Viet et al., 2012). In addition, borehole-based stress analyses have revealed significant spatial variability in the present-day stress regime across the basin (Huong et al., 2012). Future studies should integrate a broader range of geological and geomechanical constraints into the RPT calibration and spatial prediction workflow. Relevant constraints may include interpreted seismic horizons, fault architecture, structural position, proximity to major faults, depositional facies, formation-pressure data, stress-orientation indicators, and AI/ML-based prediction approaches.

Incorporating these geological and geomechanical constraints would reduce the potential for elastic-property variations to be attributed solely to depth. It would enhance the geological plausibility of RPT predictions beyond the available well control. Ultimately, such an integrated workflow could provide more robust spatial predictions of RPT-derived properties by accounting for both vertical compaction trends and lateral variations associated with geological heterogeneity.

Acknowledgements

The authors gratefully acknowledge PetroVietnam and the Vietnam Petroleum Institute (VPI) for permission to publish the data and for their support of this work.

References

Asquith G.B., Krygowski D., Gibson C.R., 2004. Basic well log analysis. Tulsa: American Association of Petroleum Geologists, 16, 305–371.

Avseth P., Johansen T.A., Bakhorji A., Mustafa H.M., 2014. Rock-physics modeling guided by depositional and burial history in low-to-intermediate-porosity sandstones. Geophysics, 79(2), D115–D121. https://doi.org/10.1190/geo2013-0226.1.

Avseth P., Mukerji T., Mavko G., 2005. Quantitative seismic interpretation: Applying rock physics tools to reduce interpretation risk (1st ed.). Cambridge University Press. https://doi.org/10.1017/CBO9780511600074.

Avseth P., Ødegaard E., 2004. Well log and seismic data analysis using rock physics templates. First break, 23(10), 37–43. https://doi.org/10.3997/1365-2397.2004017.

Breitfeld H.T., Hennig-Breitfeld J., BouDagher-Fadel M., Schmidt W.J., Meyer K., Reinprecht J., Lukie T., Cuong T.X., Hall R., Kollert N., Gough A., Ismail R., 2022. Provenance of Oligocene-Miocene sedimentary rocks in the Cuu Long and Nam Con Son basins, Vietnam and early history of the Mekong River. International Journal of Earth Sciences, 111(6), 1773–1804. https://doi.org/10.1007/s00531-022-02214-0.

Byrd R.H., Lu P., Nocedal J., Zhu C., 1995. A limited memory algorithm for bound constrained optimization. SIAM Journal on Scientific Computing, 16(5), 1190–1208. https://doi.org/10.1137/0916069.

Chai T., Draxler R.R., 2014. Root mean square error (RMSE) or mean absolute error (MAE)? Arguments against avoiding RMSE in literature. Geoscientific Model Development, 7, 1247–1250. https://doi.org/10.5194/gmd-7-1247-2014.

Chicco D., Warrens M.J., Jurman G., 2021. The coefficient of determination R-squared is more informative than SMAPE, MAE, MAPE, MSE and RMSE in regression analysis evaluation. PeerJ Computer Science, 7, e623. https://doi.org/10.7717/peerj-cs.623.

Dam M.H., Trieu N.T., Tham N.T., Phuong B.T.N., Xuan T.V., 2023. Sequence stratigraphy and petrographic characteristics of Oligocene sediments in the West trough of the Cuu Long Basin, Vietnam. Marine and Petroleum Geology, 155, 106395. https://doi.org/10.1016/j.marpetgeo.2023.106395.

De Jonge-Anderson I., Ma J., Wu X., Stow D., 2022. Determining reservoir intervals in the Bowland Shale using petrophysics and rock physics models. Geophysical Journal International, 228(1), 39–65. https://doi.org/10.1093/gji/ggab334.

Dræge A., 2010. Rock physics and resistivity depth trends - an integrated approach. SEG Technical Program Expanded Abstracts 2010, 711–715. https://doi.org/10.1190/1.3513882.

Dvorkin J., Nur A., 1996. Elasticity of high-porosity sandstones: Theory for two North-Sea data sets. Geophysics, 61(5), 1363–1370. https://doi.org/10.1190/1.1444059.

Ellis D.V., Singer J.M., 2007. Well logging for earth scientists. Dordrecht: Springer, 692, 267–288.

Fawad M., Hansen J.A., Mondol N.H., 2020. Seismic-fluid detection-a review. Earth-Science Reviews, 210, 103347. https://doi.org/10.1016/j.earscirev.2020.103347.

Giao P.H., Trang P.H., Hien D.H., Ngoc P.Q., 2021. Construction and application of an adapted rock physics template (ARPT) for characterizing a deep and strongly cemented gas sand in the Nam Con Son basin, Vietnam. Journal of Natural Gas Science and Engineering, 94, 104117. https://doi.org/10.1016/j.jngse.2021.104117.

Hill R., 1963. Elastic properties of reinforced solids: Some theoretical principles. Journal of the Mechanics and Physics of Solids, 11(5), 357–372. https://doi.org/10.1016/0022-5096(63)90036-X.

Huong N.V., Trinh P.T., Dang H.N., 2011. Trang thai ung suat kien tao hien dai khu vuc be Cuu Long (Present-day tectonic stress state in the Cuu Long Basin). Vietnam Journal of Earth Sciences, 33(3ĐB), 457–464 (in Vietnamese).

Johansen T.A., Jensen E.H., Mavko G., Dvorkin J., 2013. Inverse rock physics modeling for reservoir quality prediction. Geophysics, 78(2), M1–M18. https://doi.org/10.1190/geo2012-0215.1.

Kuster G.T., Toksöz M.N., 1974. Velocity and attenuation of seismic waves in two-phase media; Part I, Theoretical formulations. Geophysics, 39(5), 587–606. https://doi.org/10.1190/1.1440450.

Luan P.T., Thanh D.D., Oksum E., Sang L.T., 2019. Estimation of Curie point depths in the Southern Vietnam continental shelf using magnetic data. Vietnam Journal of Earth Sciences, 41(3), 216–228. https://doi.org/10.15625/0866-7187/41/3/13830.

Luthi S., 2001. Geological well logs: Their use in reservoir modeling. Springer Science & Business Media.

Mai Thanh T., Dinh Van T., Le Duc L., Tran Thi Thuy V., Ngo Thi D., 2024. Some characteristics of sediments in Cenozoic basins in Northern Vietnam: implication for Oligocene paleoclimate. Vietnam Journal of Earth Sciences, 47(1), 90–117. https://doi.org/10.15625/2615-9783/21915.

Mavko G., Mukerji T., 1995. Seismic pore space compressibility and Gassmann's relation. Geophysics, 60(6), 1743–1749. https://doi.org/10.1190/1.1443907.

Mavko G., Mukerji T., Dvorkin J., 2009. The rock physics handbook: Tools for seismic analysis of porous media. 2nd ed. Cambridge University Press. https://doi.org/10.1017/CBO9780511626753.

Morley R.J., Bui V.D., Nguyen T.T., Kullman A.J., Bird R.T., Nguyen V.K., Nguyen H.C., 2019. High-resolution Palaeogene sequence stratigraphic framework for the Cuu Long Basin, offshore Vietnam, driven by climate change and tectonics, established from sequence biostratigraphy. Palaeogeography, Palaeoclimatology, Palaeoecology, 530, 113–135. https://doi.org/10.1016/j.palaeo.2019.05.010.

Nguyen T.M., Nguyen H.P., Vu V.P., Pham T.T., Bui T.N., 2022. Seismic activity in the continental shelf of South-Central Vietnam and adjacent regions from 2005 to 2020. Vietnam Journal of Marine Science and Technology, 22(2), 143–154. https://doi.org/10.15625/1859-3097/16519.

Powers D.M.W., 2011. Evaluation: From precision, recall and F-measure to ROC,

informedness, markedness and correlation. Journal of Machine Learning Technologies, 2(1), 37–63. https://doi.org/10.48550/arXiv.2010.16061.

Pubellier M., Sautter B., 2022. Key Structural Elements around the East Vietnam Sea and implications on reconstructions: towards a clarification. Vietnam Journal of Marine Science and Technology, 22(3), 217–229. Doi: 10.15625/1859-3097/17435.

Reine C., 2017. Discovering a supermodel-A rock-Physics tutorial. CSEG Recorder, 42(2), 20–25.

Rider M.H., Kennedy M., 2011. The Geological Interpretation of Well Logs. 3rd edition. Rider-French Consulting Ltd.

Russell B., 2013. A Gassmann-consistent rock physics template. CSEG Recorder, 38(6), 22–30.

Schlumberger Limited, 1991. Log interpretation principles/applications. Schlumberger Educational Services.

Schmidt W.J., Hoang B.H., Handschy J.W., Hai V.T., Cuong T.X., Tung N.T., 2019. Tectonic evolution and regional setting of the Cuu Long Basin, Vietnam. Tectonophysics, 757, 36–57. https://doi.org/10.1016/j.tecto.2019.03.001.

Serra O., 1986. Fundamentals of well-log interpretation volume 2-The interpretation of logging data: Developments in Petroleum Science No. 15B. Elsevier/Elf Aquitaine, Amsterdam.

Sokolova M., Lapalme G., 2009. A systematic analysis of performance measures for classification tasks. Information Processing & Management, 45(4), 427–437. https://doi.org/10.1016/j.ipm.2009.03.002.

Stefaniuk D., Kachanov M., 2023. Voigt-Reuss and Hashin-Shtrikman bounds revisited. International Journal of Engineering Science, 191, 103903. https://doi.org/10.1016/j.ijengsci.2023.103903.

Viet L.T., Chinh V.V., Thang T.V., Tung V.D., Ha L.T., Huong N.T.T., Quynh B.V., 2012. Development of the tectonic structure of the Cuu Long basin in Cenozoic. Vietnam Journal of Earth Sciences, 34(2), 136–145.

Zhu C., Byrd R.H., Lu P., Nocedal J., 1997. Algorithm 778: L-BFGS-B: Fortran subroutines for large-scale bound-constrained optimization. ACM Transactions on mathematical software (TOMS), 23(4), 550–560. https://doi.org/10.1145/279232.279236.

APPENDIX: APPROACH TO DATA-DRIVEN RPT

For the sake of simplicity, we consider a matrix of two lithologies of sandstone and shale. The initial values of bulk modulus and shear modulus for each given lithology are denoted as K_{sand}, G_{sand}, K_{shale}, and G_{shale}. Then the rule of mixture can be applied to the mentioned minerals in the following manner:

$$K_{voigt} = \sum_{i=1}^{2} f_i K_i \quad \text{and} \quad G_{voigt} = \sum_{i=1}^{2} f_i G_i \qquad (\mathrm{i} = \mathrm{sand}, \mathrm{shale})$$

$$\frac{1}{K_{Reuss}} = \sum_{i=1}^{2} f_i \frac{1}{K_i} \quad \text{and} \quad \frac{1}{G_{Reuss}} = \sum_{i=1}^{2} f_i \frac{1}{G_i} \qquad (\mathrm{i} = \mathrm{sand}, \mathrm{shale})$$

Afterwards, the effective bulk modulus K_m and shear modulus G_m of the matrix are determined using the Voight-Reuss bounds through weight factors (λ_K, λ_G).

$$K_m = \lambda_K \cdot K_{voigt} + (1 - \lambda_K) \cdot K_{reuss} \qquad (5)$$

$$G_m = \lambda_G \cdot G_{voigt} + (1 - \lambda_G) \cdot G_{reuss} \qquad (6)$$

Incorporating the presence of pore space, the effective dry-rock bulk and shear moduli of the porous medium are calculated as follows (Mavko & Mukerji, 1995).

$$\frac{1}{K_{dry-MM}} = \frac{1}{K_m} + \frac{\phi}{K_\phi} \qquad (7)$$

K_m K_ϕ, ϕ denote the matrix bulk modulus, the pore space stiffness, and the given porosity, respectively. Motivated by the above relationship, an approximation of the dry shear modulus G_{dry-a} is also proposed. The equations of K_{dry-MM} and G_{dry-a} are rewritten as follows:

$$K_{dry-MM} = \frac{K_m}{1 + \phi \cdot \frac{K_m}{K_\phi}} \quad (8)$$

$$G_{dry-a} = \frac{G_m}{1 + \phi \cdot \frac{G_m}{G_\phi}} \quad (9)$$

The K_{dry-MM} and G_{dry-a} then replace traditional Hertz-Mindlin bulk-shear moduli in the soft sand model framework of Dvorkin et al. (1996).

$$K_{dry-soft} = \left(\frac{\frac{\phi}{\phi_c}}{K_{dry-MM} + \frac{4}{3} G_{dry-a}} + \frac{1 - \frac{\phi}{\phi_c}}{K_m + \frac{4}{3} G_{dry-a}} \right)^{-1} - \frac{4}{3} G_{dry-a}$$

$$G_{dry-soft} = \left[\frac{\frac{\phi}{\phi_c}}{G_{dry-a} + \frac{G_{dry-a}}{6} \left(\frac{9K_{dry-MM} + 8G_{dry-a}}{K_{dry-MM} + 2G_{dry-a}} \right)} + \frac{1 - \frac{\phi}{\phi_c}}{G_m + \frac{G_{dry-a}}{6} \left(\frac{9K_{dry-MM} + 8G_{dry-a}}{K_{dry-MM} + 2G_{dry-a}} \right)} \right]^{-1} - \frac{G_{dry-a}}{6} \left(\frac{9K_{dry-MM} + 8G_{dry-a}}{K_{dry-MM} + 2G_{dry-a}} \right)$$

For the mixture of fluids, the effective fluid bulk modulus is given:

$$K_{fl} = (K_{water} - K_{HC}) \cdot S_w + K_{HC} \quad (10)$$

Finally, the saturated bulk modulus can be calculated based on the Gassmann equation while the shear modulus is set as unchanged in terms of various fluid content

$$K_{sat} = K_{dry-soft} + \frac{\left(1 - \frac{K_{dry-soft}}{K_m}\right)^2}{\frac{\phi}{K_{fl}} + \frac{1 - \phi}{K_m} - \frac{K_{dry-soft}}{K_m^2}} \quad (11)$$

$$G_{sat} = G_{dry-soft} \quad (12)$$

Given the moduli of saturated rock, the comparison with the well data is conducted. That allows us to seek the optimal elastic parameters $\boldsymbol{X}^*$:

$$\boldsymbol{X}^* = \text{argmin} \left\{ \left(K_{sat} - K_{sat}^{log}\right)^2 + \left(G_{sat} - G_{sat}^{log}\right)^2 + \lambda (X - X_0)^2 \right\} \quad (13)$$

Where:

K_{sat}^{log}: saturated bulk modulus calculated by measured log;

G_{sat}^{log}: saturated shear modulus calculated by measured log.

The optimal elastic parameters serve to build the RPT for various depth levels based on the observed elastic parameters (superimposed on the elastic domain).